

eLISA eccentricity measurements as tracers of binary black hole formation

Atsushi Nishizawa,^{1,*} Emanuele Berti,^{1,2,†} Antoine Klein,^{1,2,‡} and Alberto Sesana^{3,§}

¹*Department of Physics and Astronomy, The University of Mississippi, University, MS 38677, USA*

²*CENTRA, Departamento de Física, Instituto Superior Técnico,*

Universidade de Lisboa, Avenida Rovisco Pais 1, 1049 Lisboa, Portugal

³*School of Physics and Astronomy, The University of Birmingham, Edgbaston, Birmingham B15 2TT, UK*

(Dated: August 22, 2016)

Up to hundreds of black hole binaries individually resolvable by eLISA will coalesce in the Advanced LIGO/Virgo band within ten years, allowing for multi-band gravitational wave observations. Binaries formed via dynamical interactions in dense star clusters are expected to have eccentricities $e_0 \sim 10^{-3}$ – 10^{-1} at the frequencies $f_0 = 10^{-2}$ Hz where eLISA is most sensitive, while binaries formed in the field should have negligible eccentricity in both frequency bands. We estimate that eLISA should always be able to detect a nonzero e_0 whenever $e_0 \gtrsim 10^{-2}$; if $e_0 \sim 10^{-3}$, eLISA should detect nonzero eccentricity for a fraction $\sim 90\%$ ($\sim 25\%$) of binaries when the observation time is $T_{\text{obs}} = 5$ (2) years, respectively. Therefore eLISA observations of black hole binaries have the potential to distinguish between field and cluster formation scenarios.

I. INTRODUCTION

With the detection of gravitational waves (GWs) by the LIGO/Virgo scientific collaboration [1], black hole (BH) binaries have entered the realm of observational astronomy. The first detected binary system (GW150914) has source-frame component masses $(m_1, m_2) = (36_{-4}^{+5}, 29_{-4}^{+4}) M_\odot$, resulting in a merger remnant of mass $62_{-4}^{+4} M_\odot$. Its estimated luminosity distance is $D_L = 410_{-180}^{+160}$ Mpc, corresponding to a redshift $z = 0.09_{-0.04}^{+0.03}$ [2]. The trigger LVT151012 is also likely to be a binary BH system with masses $(m_1, m_2) = (23_{-5}^{+18}, 13_{-3}^{+4}) M_\odot$ and luminosity distance $D_L = 1.1_{-0.5}^{+0.5}$ Gpc. These early GW observations set lower bounds on binary BH merger rates [3], raising interesting questions on the formation mechanism of compact binary systems. As summarized in the LIGO/Virgo collaboration paper discussing the astrophysical implications of the discovery [4], BH binary mergers similar to GW150914 can either result from the evolution of isolated binaries in galactic fields or from dynamical interactions in young and old dense star clusters (see [5, 6] for reviews of these formation scenarios).

Sesana [7] showed that up to hundreds of GW150914-like BH binaries individually resolvable by a space-based detector such as eLISA [8] will coalesce in the LIGO band within ten years. eLISA observations can identify the time and location of the merger with uncertainties in the merger time smaller than ~ 10 s, and sky localization accuracies that in many cases are better than 1 deg^2 . This will allow multi-wavelength electromagnetic telescopes to point the GW event in advance and to constrain models of electromagnetic emission associated with BH binary

mergers. Furthermore, BH binaries that span both the eLISA and Advanced LIGO frequency bands can yield stringent tests of modified theories of gravity that predict propagation properties different from general relativity [9, 10], and in particular of theories allowing for dipolar radiation in BH binaries [11].

The GW150914 signal does not set strong bounds on the eccentricity e of the binary. Ref. [2] quotes a preliminary constraint of $e < 0.1$ at $f = 10$ Hz. It is unlikely that Advanced LIGO observations may use eccentricity measurements to differentiate between the field and cluster scenarios: as shown e.g. in Fig. 3 of Ref. [4], binaries in the LIGO band will almost always be circular. Earth-based GW observations could only differentiate between field and cluster formation by looking at spin dynamics (see e.g. [12]), redshift distribution and possibly kicks.

However binaries formed in clusters – unlike binaries formed in the field – should have non-negligible eccentricity in the eLISA band. Here we show that eLISA could measure the eccentricity of BH binaries in the last few years or months of their inspiral, constraining their formation mechanism. As a byproduct, we also show how eccentricity affects the estimation of other binary parameters (masses, merger time, distance and sky location).

The possibility of multi-band detections of eccentric intermediate-mass BH binaries by Earth- and space-based detectors was pointed out in a series of papers by Amaro-Seoane et al. [13–15], but those papers focused on BH binaries with much larger total mass. Seto [16] recently studied eccentric BH binaries of the GW150914 type in the eLISA band, but the focus of his work was considerably different from ours. He considered monochromatic sources at frequencies $\sim 0.1 - 1$ mHz, which have negligible frequency evolution, and for which the merger will not be visible in the Advanced LIGO band. On the contrary we focus on binaries that evolve rapidly in the high-frequency band of the eLISA sensitivity window, possibly merging in the Advanced LIGO band. Seto used the quadrupole formula to estimate the signal (which for $e \lesssim 0.1$ is dominated by the second

* anishiza@olemiss.edu

† eberti@olemiss.edu

‡ aklein@olemiss.edu

§ asesana@star.sr.bham.ac.uk

harmonic, i.e. by GWs emitted at twice the orbital frequency) and estimated the binary eccentricity from the characteristic amplitude of the third harmonic of the signal. We use general relativistic waveform models and a Fisher matrix analysis to estimate errors in the measurement of the eccentricity and of other parameters characterizing the source (masses, merger time, distance and sky location). We work within the small-eccentricity waveform generation formalism proposed in [17] and further developed in [18], which is adequate to address the present problem, but we note that various groups have recently made progress in the development of models for the generation, detection and parameter estimation of GWs from eccentric binaries (see e.g. [19–26]).

In the rest of this introduction we review some literature on BH formation channels and merger rates, including recent papers that were not included in the LIGO review on this topic [27], to justify our statement that field binaries should typically be circular, while binaries formed in clusters may have residual eccentricities. A more realistic study would require astrophysical models of the mass, spin and eccentricity distribution of BH binaries in both formation channels and Bayesian model selection [28]; such an analysis is beyond the scope of this paper, where we focus mostly on the preliminary issue of parameter estimation accuracy. Then we present an executive summary of our main results on eLISA measurements of eccentricity. Finally we outline the plan of the paper for the reader’s convenience.

A. Black hole formation channels

Field binaries. Tutukov and Yungelson studied the evolution of isolated massive binaries before the discovery of the binary pulsar and predicted the formation of merging binary compact objects composed of neutron stars (NSs) and/or BHs [29, 30]. Some early population studies even predicted that binary BH mergers could dominate detection rates for ground-based GW detectors [31]. Several groups made predictions on the relative rates of BH-BH, BH-NS and NS-NS binaries over the years [32–40]. All of these predictions were largely uncertain, but as late as 2014 some studies concluded that BH-BH binary detection rates would be negligible for Advanced LIGO [41].

Belczynski et al. [42] pointed out that BH-BH binaries could dominate Advanced LIGO detection rates if a significant fraction of stars form in low-metallicity environments. This claim was refined in subsequent work using the STARTRACK code with various prescriptions for common envelope evolution, BH kicks and gravitational waveforms [43–48], as well as various prescriptions for metallicity evolution as a function of redshift. These works consistently predicted that BH mergers should dominate the rates, and that large-mass BH binaries (including total masses $\sim 60M_{\odot}$ and above) should be detectable in large numbers out to $z \sim 2$. Notably, before

the detection of GW150914 Belczynski et al. [47] found that “the most likely sources to be detected with the advanced detectors are massive BH-BH mergers with total redshifted mass $\sim 30 - 70M_{\odot}$.”

Similar conclusions were reached using other population synthesis codes [49, 50]. Eldridge and Stanway [50] found that GW150914 has a low probability of arising from a stellar population with initial metallicity $Z \gtrsim 0.01$ (or $Z \gtrsim 0.5Z_{\odot}$); when $Z = 10^{-4}$, a large fraction ($\sim 26\%$) of binary BH mergers is expected to have masses compatible with the GW measurement. Other groups suggested that common envelope evolution may not be the only way to form massive BHs. Another channel involves massive, tight binaries where mixing induced by rotation and tides transports the products of hydrogen burning throughout the stellar envelopes, enriching the entire star with helium and preventing the build-up of an internal chemical gradient [51–53]. In these scenarios there would never be a giant phase: both stars would stay within their Roche lobes and eventually form massive BHs, because the cores that collapse would be large. Yet another scenario invokes a Population III origin for massive BH binaries [54–56], but semi-analytical models suggest that the probability of GW150914 having formed in the early Universe is $\sim 1\%$ [57].

The key point for us is that *BH binaries produced in the field are expected to be circular in both the Advanced LIGO and eLISA bands*. Typical eccentricity distributions for BH binaries at frequencies ~ 0.3 Hz are shown in Fig. 5 of [58]; predicted values are in the range $10^{-6} \lesssim e \lesssim 10^{-4}$. Massive BH binaries of interest for multi-band astronomy are at the heavy end of the mass spectrum, so they should receive small kicks (see e.g. Sec. 6 of [47]) and be on the small-eccentricity side of the distributions predicted in [58]. For all practical purposes, massive BH binaries formed in the field can be assumed to be circular in the eLISA band.

Dense star clusters. A different scenario for binary BH formation involves dense star clusters [59, 60]. In these environments BHs quickly become the most massive objects. They sink towards the cluster core, form pairs through dynamical interactions, and they are most commonly ejected in binary configurations with inspiral times shorter than the age of the Universe. This basic scenario was refined by various authors [61–77].

A dynamical effect that can produce large eccentricities in the LIGO band is the Kozai mechanism [78]. Recent studies of Kozai-Lidov resonances showed that binary BH mergers may be more likely inside the radius of influence of supermassive BHs in galactic centers [79, 80] or in hierarchical triples [81, 82]. More work is required to understand whether these events can lead to rates comparable to the other formation channels, and also to establish the conditions (masses, inclinations, semi-major axes and eccentricities of both the inner and outer binary) that could result in non-negligible eccentricities in the eLISA band.

Some predictions for the eccentricity distribution of dynamically formed binaries can be found in Fig. 10 of [74].

The eccentricity at 10 Hz of BH binaries merging at $z < 1$ in the capture scenario peaks at $e = 10^{-6}$, with most of the sources having $e < 10^{-5}$. The classic results by Peters and Mathews [83] imply that, so long as $e \ll 1$, $e \sim f^{-19/18} \approx f^{-1}$ (see e.g. Fig. 1 of [84]). Here we focus on sources emitting at $f > f_0 = 10^{-2}$ Hz in the eLISA band. Their typical eccentricity at frequency $f \sim f_0$ is thus $e \sim 10^{-3}$, with most sources having $e \lesssim 10^{-2}$. Almost all relevant eLISA sources (both resolvable and unresolvable) are at $f > 10^{-3}$ Hz, and their expected eccentricity is $e \lesssim 0.1$. These numbers are large enough to require eccentric templates for matched filtering, but the amplitude and phasing of the signal for binaries with $e \lesssim 0.1$ can be treated in a small-eccentricity approximation. To summarize: extrapolating the results in Ref. [74] to lower frequencies, we expect dynamically formed BH binaries to have small but non-negligible eccentricities $e \lesssim 0.1$ in the eLISA band, and therefore a small-eccentricity approximation is adequate to study this problem.

B. Executive summary

Consider a binary system with component masses (in the source frame) m_1 and m_2 , total mass $M = m_1 + m_2$, symmetric mass ratio $\eta = m_1 m_2 / M^2$ and chirp mass $\mathcal{M} = \eta^{3/5} M$. Assume that the binary is located at redshift z – or equivalently, for a given cosmological model, at luminosity distance $D_L = D_L(z)$ – so that the redshifted chirp mass $\mathcal{M}_z = (1+z)\mathcal{M}$, the redshifted total mass $M_z = (1+z)M$, and similarly for the other mass parameters. Two angles $(\bar{\theta}_S, \bar{\phi}_S)$ specify the direction of the source in the solar barycenter frame, and for convenience we introduce $R = 1$ AU. Let t_c be the coalescence time, ϕ_c the coalescence phase, \mathbf{L} the binary’s orbital angular momentum vector (with $\hat{\mathbf{L}} = \mathbf{L}/|\mathbf{L}|$ the corresponding unit vector), and $\hat{\mathbf{N}}$ a unit vector pointing in the source direction as measured in the solar barycenter frame. Furthermore, let $\chi = f/f_0$ be the frequency normalized to a reference frequency – here chosen to be $f_0 = 10^{-2}$ Hz – where the eccentricity is $e(f_0) = e_0$, and introduce the standard post-Newtonian (PN) parameter $x = (\pi M_z f)^{2/3}$.

We model eLISA as two independent interferometers with non-orthogonal arms. The sky-averaged noise power spectral density for each of the two interferometers is denoted by $NiAj$, as in [85]; here $i = 1, 2$ refers to different acceleration noise baselines, and $j = 1, 5$ denotes different armlengths (1 or 5 Gm). The observation time T_{obs} is chosen to be either 5 or 2 years. This choice significantly affects the signal-to-noise ratio (SNR): if, following [7], we adopt a fiducial 5-year observation time and assume that the binary merges at the end of the observation, the initial frequency of the binary will be

$$f_{\text{min}} = 0.015 \left(\frac{30 M_\odot}{\mathcal{M}_z} \right)^{5/8} \left(\frac{5 \text{ yr}}{T_{\text{obs}}} \right)^{3/8} \text{ Hz}, \quad (1)$$

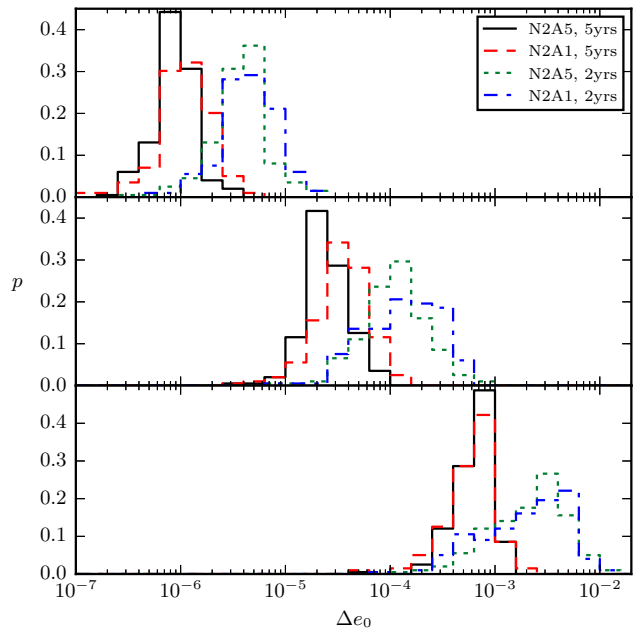


Figure 1. Parameter estimation errors on the eccentricity e_0 at frequency $f_0 = 10^{-2}$ Hz using “full eccentric” waveforms for nonspinning binaries. Different panels refer to catalogs with $e_0 = 0.1, 0.01$ and 0.001 (from top to bottom). The various linestyles refer to different noise curves and observation times: N2A5 and $T_{\text{obs}} = 5$ yrs (solid black), N2A1 and $T_{\text{obs}} = 5$ yrs (dashed red), N2A5 and $T_{\text{obs}} = 2$ yrs (dotted green), N2A1 and $T_{\text{obs}} = 2$ yrs (dash-dotted blue).

where we scaled the result by the estimated redshifted chirp mass of GW150914. Our SNR and Fisher matrix calculations are truncated at a maximum frequency $f_{\text{max}} = 1$ Hz, beyond which the eLISA noise is not expected to be under control.

Our main results on eccentricity measurements are summarized in Figs. 1 and 2. Their behavior can be understood, at least qualitatively, using simple scaling arguments. Neglecting correlations between parameters, in a Fisher matrix approximation the error on e_0 is

$$\Delta e_0 \sim \left[f \frac{|\partial_{e_0} \tilde{h}|^2}{S_h} \right]^{-1/2}, \quad (2)$$

where \tilde{h} denotes the Fourier transform of the GW amplitude and $S_h(f)$ is the noise power spectral density of the detector. To leading order in a small-eccentricity expansion (what we call the “restricted eccentric waveform” in Section III A below) and in the stationary phase approximation, corrections due to the eccentricity enter only in the GW phase through the term proportional to e_0^2 in Eq. (8) below, and therefore $\partial_{e_0} \tilde{h} = \mathcal{M}_z^{-5/6} f^{-89/18} e_0$. Let us approximate the frequency dependence of the noise power spectral density by a power law, $S_h \sim f^{2\alpha}$. Since the dominant contribution to the Fisher matrix

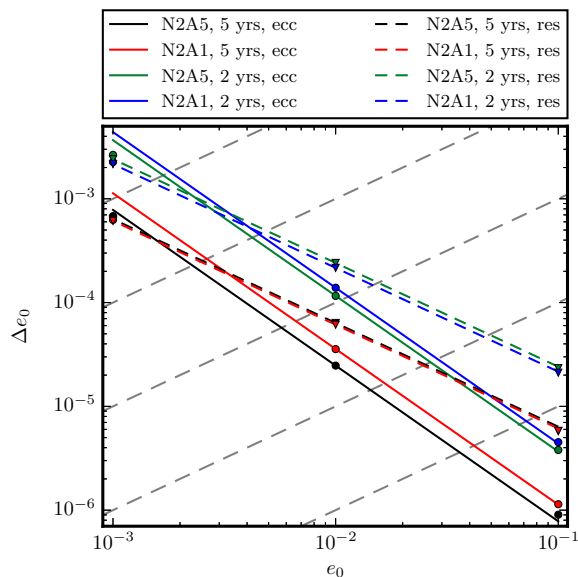


Figure 2. Scaling of the median error Δe_0 with e_0 for the N2A5 noise model. Dashed (solid) lines correspond to restricted (full) eccentric waveforms, respectively. Colors refer to N2A5 and $T_{\text{obs}} = 5$ yrs (black), N2A1 and $T_{\text{obs}} = 5$ yrs (red), N2A5 and $T_{\text{obs}} = 2$ yrs (green), N2A1 and $T_{\text{obs}} = 2$ yrs (blue). From top left to bottom right, gray long-dashed lines correspond to $\Delta e_0/e_0 = 1, 10^{-1}, 10^{-2}, 10^{-3}, 10^{-4}$.

comes from the lowest frequencies, from Eq. (2) we have

$$\begin{aligned} \Delta e_0 &\sim \mathcal{M}_z^{5/6} f_{\text{min}}^{40/9+\alpha} e_0^{-1} \\ &\sim \mathcal{M}_z^{-5(28+9\alpha)/72} T_{\text{obs}}^{-(40+9\alpha)/24} e_0^{-1}, \end{aligned} \quad (3)$$

where on the second line we estimated f_{min} for a given observation time T_{obs} using the quadrupole formula (1) for a circular binary. In summary, to leading order we expect a rough scaling law of the form

$$\Delta e_0 \sim \mathcal{M}_z^{-\gamma_m} T_{\text{obs}}^{-\gamma_t} e_0^{-\gamma_e}, \quad (4)$$

with $(\gamma_m, \gamma_t) = (2.57, 2.04)$ for $\alpha = 1$ (N2A5 and N2A1, 2yrs), $(\gamma_m, \gamma_t) = (2.19, 1.82)$ for $\alpha = 0.4$ (N2A1, 5yrs) and $\gamma_e = 1$. Note that α depends not only on the noise curve, but also on f_{min} , that is lower for longer T_{obs} : the frequency dependence of the eLISA noise curve is flatter when we consider N2A1 and a 5-year observation time.

This rough approximation will break down when the SNR is small (so the Fisher matrix approximation is invalid), correlations cannot be neglected (as is the case for the “restricted” eccentric waveform), or eccentricities are too small and therefore not measurable. In practice we carry out numerical calculations using the “full” eccentric waveform described in Section III B below. Obtaining analytical estimates in this case is more complicated due to the existence of frequency sidebands, but by fitting our numerical data we found that the scaling law with \mathcal{M}_z holds well also for these full eccentric waveforms. Because of the breaking of some parameter degeneracies,

noise	T_{obs}	ϵ_0	γ_m	γ_e
N2A1	2yr	1.0×10^{-5}	2.57	1.5
N2A1	5yr	2.2×10^{-6}	2.19	1.5
N2A5	2yr	6.5×10^{-6}	2.57	1.5
N2A5	5yr	9.0×10^{-7}	2.57	1.5

Table I. Fitting parameters in the scaling relation of Eq. (5).

the scaling with e_0 is modified from the previous simple prediction: $\gamma_e \approx 1.5$ for $e_0 > 0.01$. A more accurate scaling law obtained by fitting our numerical data is

$$\Delta e_0 \approx \epsilon_0 \left(\frac{d_L}{400 \text{ Mpc}} \right) \left(\frac{30 M_\odot}{\mathcal{M}_z} \right)^{\gamma_m} \left(\frac{0.1}{e_0} \right)^{\gamma_e}, \quad (5)$$

where the fitting parameters $(\epsilon_0, \gamma_m, \gamma_e)$ are listed in Table I. This scaling is further illustrated in Fig. 2.

The simple scalings of Eqs. (4) and (5) are helpful to understand the numerical results shown in Fig. 1. The error Δe_0 gets larger with decreasing eccentricity: when $e_0 \sim 0.1$ the typical error is $\Delta e_0 \approx 10^{-6}$, but when $e_0 \sim 0.001$ the typical error $\Delta e_0 \sim e_0$. For a given noise curve (N2A5 or N2A1), as expected, longer observation times lead to smaller errors. The effect of changing the armlength is sensibly milder, but (everything else being equal) 5 Gm configurations (A5) yield slightly smaller errors than 1 Gm configurations (A1).

Recall from our previous discussion that binaries formed in dense star clusters are expected to have eccentricities $10^{-3} \lesssim e_0 \lesssim 10^{-2}$ at the frequencies $f_0 = 10^{-2}$ Hz where eLISA is most sensitive, while binaries formed in the field should have negligible eccentricity $10^{-6} \lesssim e \lesssim 10^{-4}$ at these frequencies. eLISA should always be able to detect a nonzero e_0 whenever $e_0 \gtrsim 10^{-2}$; if $e_0 \sim 10^{-3}$, we find that eLISA will detect nonzero eccentricity for a fraction $\sim 90\%$ ($\sim 25\%$) of binaries when $T_{\text{obs}} = 5$ (2) years, respectively. Therefore eLISA observations of GW150914-like BH binaries have the potential to distinguish between field and cluster formation scenarios. This is the main result of our paper.

C. Plan of the paper

The rest of the paper provides details on the source catalogs used for our Monte Carlo simulations, on our waveform models, and on the parameter estimation errors for other source parameters (including masses, distance and sky location). In Section II we describe how we generate the source catalogs used in our Monte Carlo analysis. In Section III we describe our “restricted” and “full” eccentric waveform models. In Section IV we show how eccentricity affects errors on the other parameters (time of merger, masses, distance and sky location). We conclude with possible directions for future work. Finally, in Appendix A we show that confusion noise is

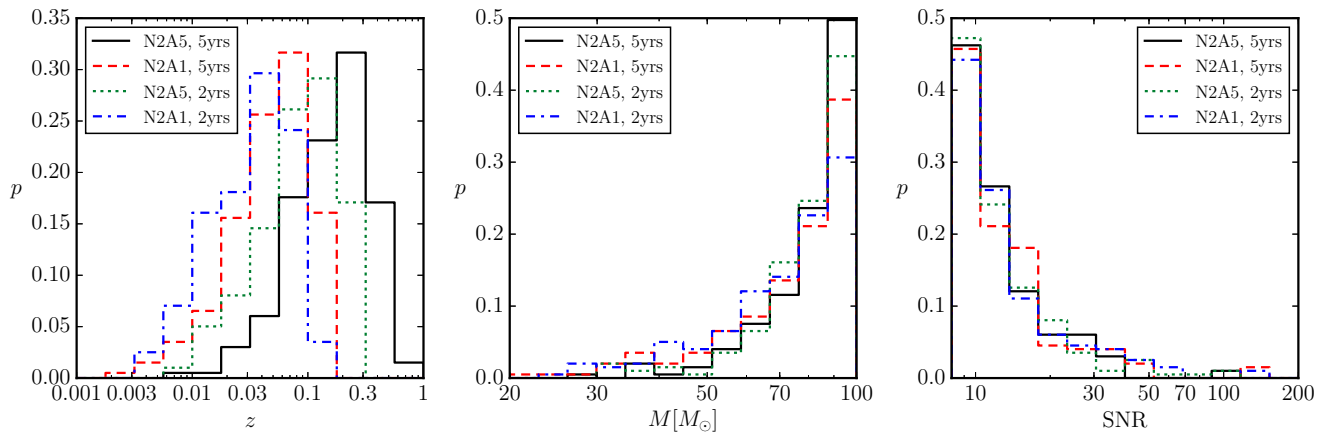


Figure 3. Distribution of parameters (from left to right: redshift, mass and SNR) for the source catalogs used in our Monte Carlo parameter estimation study. The various linestyles correspond to N2A5 and $T_{\text{obs}} = 5$ yrs (solid black), N2A1 and $T_{\text{obs}} = 5$ yrs (dashed red), N2A5 and $T_{\text{obs}} = 2$ yrs (dotted green), N2A1 and $T_{\text{obs}} = 2$ yrs (dash-dotted blue).

unlikely to affect our parameter estimation calculations. In the whole paper we use geometrical units ($c = G = 1$).

II. SOURCE CATALOGS

Following the LIGO/Virgo paper on rate estimates [3], we randomly draw the masses of the two BHs m_1 and m_2 from a log-flat mass distribution in the range $5 M_{\odot} < m_i < 100 M_{\odot}$, with the additional requirement that $M < 100 M_{\odot}$. The binary’s sky location and the orientation of the angular momentum are distributed uniformly over the sky. The source redshift is randomly selected assuming a constant binary BH merger rate and the Lambda-Cold-Dark-Matter (Λ CDM) flat cosmological model with $\Omega_m = 0.3$, $\Omega_{\Lambda} = 1 - \Omega_m$ and $H_0 = 72 \text{ km s}^{-1} \text{ Mpc}^{-1}$ [86]. For each binary we can compute the SNR ρ , defined as

$$\rho^2 \equiv 4 \int_{f_{\min}}^{f_{\max}} \frac{|\tilde{h}(f)|^2}{S_h(f)} df, \quad (6)$$

where we use analytical approximations to the N2A1 and N2A5 noise power spectral densities $S_h(f)$ [85]. When computing SNRs we fix the reference eccentricity e_0 to zero: corrections due to nonzero e_0 are of order e_0^2 , and they are less than 1% for the fiducial values $e_0 \leq 0.1$ considered in this paper.

We generate $N_s = 500$ binary BH sources that are observable by eLISA by imposing a detection threshold $\rho > 8$ for each observation period and noise curve. The mass, redshift and SNR distributions of the events generated in this way are shown in Fig. 3, and the medians of these quantities are listed in Table II. The SNR and mass distributions are very similar in all four cases, due to the chosen detection threshold in SNR and to the relatively limited mass range for the binary components, respectively. With higher detector sensitivity and longer observation times (corresponding to smaller f_{\min}) it is

noise	T_{obs}	\bar{N}	95%	\bar{z}	\bar{M}	$\bar{\rho}$
N2A1	2yr	2	0–8	0.0353	78.9	11.1
N2A1	5yr	4	0–14	0.0494	80.7	11.0
N2A5	2yr	30	5–121	0.0803	82.8	10.6
N2A5	5yr	106	13–348	0.170	85.0	10.9

Table II. Bulk properties of the Monte Carlo distributions chosen for our study. \bar{N} denotes the median (and “95%” the 95% confidence interval) of eLISA detections, given current uncertainties in binary BH merger rates. The last three columns list median values for the redshift, total mass and SNR.

possible to detect sources at higher redshifts, because the GW amplitude $\tilde{h} \sim \mathcal{M}_z^{5/6} f^{-7/6} D_L^{-1} \sim \mathcal{M}^{5/6} f^{-7/6} z^{-1}$ at small redshifts. Note that the tail of the redshift distribution extends below $z = 0.01$, corresponding to ~ 40 Mpc, below which the galaxy distribution is not continuous. The number of sources we simulated ($N_s = 500$) was chosen arbitrarily to study probability distributions in parameter estimation accuracy. The absolute number of observed events depends, of course, on binary BH merger rates. In Table II we list the median \bar{N} and 95% confidence interval of expected eLISA detections for each assumed noise curve and mission duration.

III. ECCENTRIC BINARY WAVEFORMS

The most accurate Fourier-domain eccentric waveforms available at present were computed by Yunes et al. [17] and Tanay et al. [18] in the small-eccentricity approximation, i.e. using a power series expansion in e_0 . The waveforms in [17] are accurate up to (Newtonian, e_0^8) order in amplitude and (Newtonian, e_0^6) order in phase. The waveforms in [18] used here are accurate up to (Newtonian, e_0^6) order in amplitude and (2PN, e_0^6)

order in phase. The waveform phase calculation has recently been extended up to 3PN by Moore et al. [25]; however their calculation is limited to e_0^0 order in amplitude and e_0^2 order in phase. The waveforms in [17, 18] are more accurate for our present purposes, because eLISA observes the low-frequency early inspiral of a BH binary, where eccentricity is larger (recall that $e \propto f^{-19/18}$) and PN effects are relatively less important.

As discussed in the introduction, the sources we are interested in are expected to have eccentricities $e_0 \lesssim 0.1$ at frequencies $f_0 = 10^{-2}$ Hz, roughly corresponding to the “bucket” of eLISA’s sensitivity window. Therefore we are justified in using the small-eccentricity waveform generation formalism proposed in [17] and developed in [18]. Nonspinning eccentric waveforms depend on ten physical parameters $\{\mathcal{M}_z, \eta, t_c, \phi_c, D_L, e_0, \theta_L, \bar{\phi}_L, \bar{\theta}_S, \bar{\phi}_S\}$: redshifted chirp mass, symmetric mass ratio, time and phase at coalescence, luminosity distance, eccentricity at 10^{-2} Hz, two angles describing the direction of the orbital angular momentum, and two angles corresponding to the orientation of the source in the sky. The angular variables are measured in the solar barycentric frame. This eccentric waveform is, in general, quite complicated, and for our parameter estimation calculations we will further expand the frequency-domain waveforms, first including only phase corrections up to leading order in eccentricity (what we will refer to as the “restricted eccentric” case, Section III A), and then including up to next-to-leading order phase corrections as well as amplitude modulations (“full eccentric” case, Section III B). As we will see, restricted eccentric waveforms are useful to gain analytical understanding of the effects due to nonzero eccentricity, but they are insufficient for parameter estimation. This happens mainly because restricted waveforms do not include frequency sidebands to the dominant harmonic at $f = 2f_{\text{orb}}$. These sidebands, which are present in the “full eccentric” waveforms, carry crucial information that is necessary to break parameter degeneracies.

A. Restricted eccentric waveforms

The Fourier transform of the 2PN restricted gravitational waveform for a nonspinning circular binary with an eccentric-orbit phase correction reads [87]

$$\tilde{h}(f) = \frac{A}{D_L(z)} \mathcal{M}_z^{5/6} f^{-7/6} e^{i\Psi(f)} \left\{ \frac{5}{4} \mathcal{F}_\alpha [t(f)] \right\} e^{-i\varphi_D[t(f)]}, \quad (7)$$

where the amplitude $A = 1/(\sqrt{6}\pi^{2/3})$ includes a factor $\sqrt{3}/2$ because eLISA’s arms have an opening angle of 60° , as well as a $\sqrt{3}/20$ factor needed to use a sky-averaged sensitivity [88]. Denoting the α th detector’s response functions by F_α^+ and F_α^\times , the unit vector of orbital angular momentum by $\hat{\mathbf{L}}$, the unit vector directed to the source by $\hat{\mathbf{N}}$, and the phase of the detector’s orbital mo-

tion by $\bar{\phi}$, the phasing is given by

$$\begin{aligned} \Psi(f) = & 2\pi f t_c - \phi_c - \frac{\pi}{4} + \frac{3}{128} (\pi \mathcal{M}_z f)^{-5/3} \\ & \times \left[1 - \frac{2355}{1462} e_0^2 \chi^{-19/9} + \frac{20}{9} \left(\frac{743}{336} + \frac{11}{4} \eta \right) x \right. \\ & \left. - 16\pi x^{3/2} + \left(\frac{15293365}{508032} + \frac{27145}{504} \eta + \frac{3085}{72} \eta^2 \right) x^2 \right], \quad (8) \end{aligned}$$

$$\mathcal{F}_\alpha(t) = \left\{ 1 + (\hat{\mathbf{L}} \cdot \hat{\mathbf{N}})^2 \right\} F_\alpha^+(t) - 2i(\hat{\mathbf{L}} \cdot \hat{\mathbf{N}}) F_\alpha^\times(t), \quad (9)$$

$$\varphi_D(t) = 2\pi f(t) R \sin \bar{\theta}_S \cos[\bar{\phi}(t) - \bar{\phi}_S], \quad (10)$$

where $R = 1$ AU. The time variable t is related to the frequency f by

$$\begin{aligned} t(f) = & t_c - \frac{5}{256} \mathcal{M}_z (\pi \mathcal{M}_z f)^{-8/3} \\ & \times \left[1 - \frac{157}{43} \frac{e_0^2}{\chi^{19/9}} + \frac{4}{3} \left(\frac{743}{336} + \frac{11}{4} \eta \right) x - \frac{32\pi}{5} x^{3/2} \right. \\ & \left. + \left(\frac{3058673}{508032} + \frac{5429}{504} \eta + \frac{617}{72} \eta^2 \right) x^2 \right]. \quad (11) \end{aligned}$$

B. Full eccentric waveforms

A better approximation to the Fourier transform of the gravitational waveform for a nonspinning eccentric binary is [17, 18]

$$\tilde{h}(f) = \sum_{\ell=1}^{10} \tilde{h}_\ell(f), \quad (12)$$

$$\begin{aligned} \tilde{h}_\ell(f) = & \frac{A}{D_L(z)} \mathcal{M}_z^{5/6} f^{-7/6} e^{i\Psi_\ell(f)} \\ & \times \left\{ \frac{5}{8} \xi_\ell [t(f)] \left(\frac{\ell}{2} \right)^{2/3} \right\} e^{-i\varphi_{D,\ell}[t(f)]}, \quad (13) \end{aligned}$$

where

$$\xi_\ell(t) = \frac{(1 - e^2)^{7/4}}{(1 + \frac{73}{24} e^2 + \frac{37}{96} e^4)^{1/2}} \{ \Gamma_\ell(t) + i \Sigma_\ell(t) \}, \quad (14)$$

$$\Gamma_\ell(t) = F_\alpha^+(t) C_+^{(\ell)} + F_\alpha^\times(t) C_\times^{(\ell)}, \quad (15)$$

$$\Sigma_\ell(t) = F_\alpha^+(t) S_+^{(\ell)} + F_\alpha^\times(t) S_\times^{(\ell)}, \quad (16)$$

$$\varphi_{D,\ell}(t) = 2\pi \frac{2f}{\ell} R \sin \bar{\theta}_S \cos[\bar{\phi}(t) - \bar{\phi}_S]. \quad (17)$$

The coefficients $C_+^{(\ell)}$, $C_\times^{(\ell)}$, $S_+^{(\ell)}$, $S_\times^{(\ell)}$ depend on the eccentricity e and on the inclination angle ι , and they are given in [17] (where the azimuthal angle determining the position of the detector relative to the source, β in the notation of [17, 19], is set to zero). Here we assume $e_0 \ll 1$

and retain terms up to $O(e_0^2)$, with the following result: where

$$\tilde{h}_2(f) = \frac{A}{D_L(z)} \mathcal{M}_z^{5/6} f^{-7/6} e^{i\Psi_2(f)} \left\{ \frac{5}{4} \mathcal{F}_\alpha[t(f)] \right\} e^{-i\varphi_{D,2}[t(f)]}, \quad q_1(t) = \left(\frac{1}{2} \right)^{8/3} \chi^{-19/18} e_0 \left[3 - \frac{2\{1 - (\hat{\mathbf{L}} \cdot \hat{\mathbf{N}})^2\} F_\alpha^+(t) \mathcal{F}_\alpha^*(t)}{|\mathcal{F}_\alpha(t)|^2} \right], \quad (18)$$

$$\tilde{h}_1(f) = q_1[f, t(f)] e^{i[\Psi_1(f) - \Psi_2(f)]} \tilde{h}_2(f) e^{-i\varphi_{D,1}[t(f)]}, \quad q_3 = \left(\frac{3}{2} \right)^{8/3} \chi^{-19/18} e_0. \quad (19)$$

$$\tilde{h}_3(f) = q_3(f) e^{i[\Psi_3(f) - \Psi_2(f)]} \tilde{h}_2(f) e^{-i\varphi_{D,3}[t(f)]}, \quad (20) \quad \text{The 2PN phase up to } O(e_0^2) \text{ is [18]}$$

$$\begin{aligned} \Psi_\ell(f) = & 2\pi f t_c - \frac{\ell}{2} \phi_c - \frac{\pi}{4} + \frac{3}{128} \left(\frac{\ell}{2} \right)^{8/3} (\pi \mathcal{M}_z f)^{-5/3} \left[1 - \frac{2355}{1462} e_0^2 \chi^{-19/9} \right. \\ & + x \left\{ \frac{3715}{756} + \frac{55}{9} \eta + \left(\left(-\frac{2045665}{348096} - \frac{128365}{12432} \eta \right) \chi^{-19/9} + \left(-\frac{2223905}{491232} + \frac{154645}{17544} \eta \right) \chi^{-25/9} \right) e_0^2 \right\} \\ & + x^{3/2} \left\{ -16\pi + \left(\frac{65561\pi}{4080} \chi^{-19/9} - \frac{295945\pi}{35088} \chi^{-28/9} \right) e_0^2 \right\} \\ & + x^2 \left\{ \frac{15293365}{508032} + \frac{27145}{504} \eta + \frac{3085}{72} \eta^2 + \left(-\frac{111064865}{14141952} - \frac{165068815}{4124736} \eta - \frac{10688155}{294624} \eta^2 \right) \chi^{-19/9} e_0^2 \right. \\ & \left. + \left(-\frac{5795368945}{350880768} + \frac{4917245}{1566432} \eta + \frac{25287905}{447552} \eta^2 \right) \chi^{-25/9} e_0^2 + \left(\frac{936702035}{1485485568} + \frac{3062285}{260064} \eta - \frac{14251675}{631584} \eta^2 \right) \chi^{-31/9} e_0^2 \right\} \left. \right]. \quad (23) \end{aligned}$$

The relation between time and frequency up to 2PN can be derived from Eq. (B8a) in [18]. Keeping terms up to

$O(e_0^2)$, we can integrate dF/dt and obtain $t(F)$. Setting $F = f/\ell$ with $\ell = 2$, we have

$$\begin{aligned} t(f) = & t_c - \frac{5}{256} \mathcal{M}_z (\pi \mathcal{M}_z f)^{-8/3} \left[1 - \frac{157}{43} e_0^2 \chi^{-19/9} \right. \\ & + x \left\{ \frac{743}{252} + \frac{11}{3} \eta + \left(\left(-\frac{409133}{37296} - \frac{25673}{1332} \eta \right) \chi^{-19/9} + \left(-\frac{444781}{43344} + \frac{30929}{1548} \eta \right) \chi^{-25/9} \right) e_0^2 \right\} \\ & + x^{3/2} \left\{ -\frac{32}{5} \pi + \left(\frac{65561\pi}{2448} \chi^{-19/9} - \frac{59189\pi}{3096} \chi^{-28/9} \right) e_0^2 \right\} \\ & + x^2 \left\{ \frac{3058673}{508032} + \frac{5429}{504} \eta + \frac{617}{72} \eta^2 + \left(-\frac{22212973}{1928448} - \frac{33013763}{562464} \eta - \frac{2137631}{40176} \eta^2 \right) e_0^2 \chi^{-19/9} \right. \\ & \left. + \left(-\frac{1159073789}{37594368} + \frac{983449}{167832} \eta + \frac{5057581}{47952} \eta^2 \right) e_0^2 \chi^{-25/9} + \left(\frac{187340407}{131072256} + \frac{10411769}{390096} \eta - \frac{2850335}{55728} \eta^2 \right) e_0^2 \chi^{-31/9} \right\} \left. \right]. \quad (24) \end{aligned}$$

IV. PARAMETER ESTIMATION ERRORS

Median values of the parameter estimation errors for nonspinning binaries under different assumptions on the eLISA detector noise and on the observation time are listed in Table III for restricted eccentric waveforms, and in Table IV for full eccentric waveforms.

Let us focus first on the restricted eccentric parameter estimation results of Table III. The phasing of the inspiral signal observed by eLISA is predominantly determined by the mass parameters, which are therefore estimated very well in most cases. The signal is also modulated by the detector's orbital motion in a way that depends on the position of the source. This allows us to deter-

noise	T_{obs}	e_0	$\Delta \log \mathcal{M}$	$\Delta \log \eta$	Δt_c [s]	$\Delta \log D_L$	Δe_0	$\Delta \Omega_S$ [deg ²]
N2A1	2yr	0	1.49×10^{-6}	6.82×10^{-3}	1.52	0.438	—	1.06×10^{-1}
		10^{-3}	6.97×10^{-6}	3.02×10^{-2}	2.74	0.438	2.16×10^{-3}	1.42×10^{-1}
		10^{-2}	6.97×10^{-6}	3.02×10^{-2}	2.74	0.438	2.16×10^{-4}	1.42×10^{-1}
		10^{-1}	7.01×10^{-6}	3.03×10^{-2}	2.75	0.437	2.11×10^{-5}	1.42×10^{-1}
N2A1	5yr	0	5.62×10^{-7}	2.87×10^{-3}	1.75	0.469	—	1.39×10^{-1}
		10^{-3}	3.32×10^{-6}	1.51×10^{-2}	2.25	0.469	6.12×10^{-4}	1.60×10^{-1}
		10^{-2}	3.32×10^{-6}	1.51×10^{-2}	2.25	0.469	6.12×10^{-5}	1.60×10^{-1}
		10^{-1}	3.34×10^{-6}	1.54×10^{-2}	2.26	0.469	5.81×10^{-6}	1.61×10^{-1}
N2A5	2yr	0	2.14×10^{-6}	1.10×10^{-2}	2.29	0.473	—	1.29×10^{-1}
		10^{-3}	1.05×10^{-5}	5.02×10^{-2}	5.11	0.473	2.41×10^{-3}	1.86×10^{-1}
		10^{-2}	1.05×10^{-5}	5.02×10^{-2}	5.11	0.473	2.41×10^{-4}	1.86×10^{-1}
		10^{-1}	1.06×10^{-5}	5.06×10^{-2}	5.13	0.473	2.33×10^{-5}	1.86×10^{-1}
N2A5	5yr	0	9.01×10^{-7}	5.07×10^{-3}	3.17	0.529	—	2.32×10^{-1}
		10^{-3}	5.80×10^{-6}	2.86×10^{-2}	4.36	0.529	6.37×10^{-4}	3.03×10^{-1}
		10^{-2}	5.80×10^{-6}	2.87×10^{-2}	4.37	0.534	6.36×10^{-5}	3.04×10^{-1}
		10^{-1}	5.85×10^{-6}	2.80×10^{-2}	4.37	0.530	5.78×10^{-6}	3.05×10^{-1}

Table III. Median parameter estimation errors with restricted eccentric waveforms.

noise	T_{obs}	e_0	$\Delta \log \mathcal{M}$	$\Delta \log \eta$	Δt_c [s]	$\Delta \log D_L$	Δe_0	$\Delta \Omega_S$ [deg ²]
N2A1	2yr	0	1.49×10^{-6}	6.82×10^{-3}	1.52	0.438	—	1.06×10^{-1}
		10^{-3}	7.30×10^{-6}	3.14×10^{-2}	2.71	0.436	2.26×10^{-3}	1.19×10^{-1}
		10^{-2}	5.00×10^{-6}	2.16×10^{-2}	2.13	0.436	1.39×10^{-4}	1.10×10^{-1}
		10^{-1}	1.07×10^{-6}	4.60×10^{-3}	1.43	0.432	4.52×10^{-6}	1.02×10^{-1}
N2A1	5yr	0	5.62×10^{-7}	2.87×10^{-3}	1.75	0.469	—	1.39×10^{-1}
		10^{-3}	3.55×10^{-6}	1.57×10^{-2}	2.27	0.469	6.26×10^{-4}	1.51×10^{-1}
		10^{-2}	2.05×10^{-6}	8.52×10^{-3}	1.94	0.464	3.56×10^{-5}	1.41×10^{-1}
		10^{-1}	4.10×10^{-7}	1.92×10^{-3}	1.72	0.450	1.14×10^{-6}	1.35×10^{-1}
N2A5	2yr	0	2.14×10^{-6}	1.10×10^{-2}	2.29	0.473	—	1.29×10^{-1}
		10^{-3}	1.09×10^{-5}	5.52×10^{-2}	5.71	0.473	2.65×10^{-3}	1.43×10^{-1}
		10^{-2}	5.87×10^{-6}	2.70×10^{-2}	3.43	0.473	1.16×10^{-4}	1.34×10^{-1}
		10^{-1}	1.21×10^{-6}	6.12×10^{-3}	2.23	0.463	3.80×10^{-6}	1.26×10^{-1}
N2A5	5yr	0	9.01×10^{-7}	5.07×10^{-3}	3.17	0.529	—	2.32×10^{-1}
		10^{-3}	6.29×10^{-6}	3.06×10^{-2}	4.45	0.529	6.81×10^{-4}	2.44×10^{-1}
		10^{-2}	2.37×10^{-6}	1.14×10^{-2}	3.54	0.525	2.47×10^{-5}	2.33×10^{-1}
		10^{-1}	5.04×10^{-7}	2.83×10^{-3}	3.14	0.505	9.04×10^{-7}	2.25×10^{-1}

Table IV. Median parameter estimation errors with full eccentric waveforms.

mine the sky location of the source and, to some limited level of accuracy, also the luminosity distance D_L (see e.g. [89, 90]). For restricted eccentric waveforms e_0 enters only in the phasing [cf. Eq. (8)], and therefore it has large correlations with the mass parameters \mathcal{M} and η . As a consequence the median errors on \mathcal{M} and η are degraded by a factor of 4–6 with respect to the circular case when $e_0 \neq 0$. The estimation errors on the merger time Δt_c and sky location $\Delta \Omega_S$ also get worse by several tens of per cent, but the degradation in accuracy due to eccentricity is not as large as in the case of the mass parameters. Quite remarkably, this degradation in parameter estimation is independent of e_0 : the high correlation between the eccentricity and the mass parameters is not broken by increasing e_0 from 10^{-3} to 10^{-1} .

As shown in Table IV, this is not the case for full eccentric waveforms: the additional structure in the amplitude

and phase due to higher-order effects is crucial to break the degeneracies. Once again, a nonzero eccentricity reduces the accuracy in measuring the other parameters, in particular \mathcal{M} or η , whose determination is degraded by a factor of 4–7 with respect to the circular case when $e_0 = 10^{-3}$. However, in stark contrast with the restricted waveform, as we increase e_0 the correlations are partially broken, and the errors on all parameters (including e_0 itself: cf. Fig. 1 above) become smaller. In fact, for $e_0 = 0.1$ the accuracy in determining the mass parameters becomes slightly better than in the circular case. A qualitatively similar (but quantitatively smaller) improvement is seen in other parameter errors, such as Δt_c and $\Delta \Omega_S$.

Histograms of Δe_0 for full eccentric waveforms were shown in the introduction (Fig. 1), where we presented analytical arguments to justify why Δe_0 decreases as the

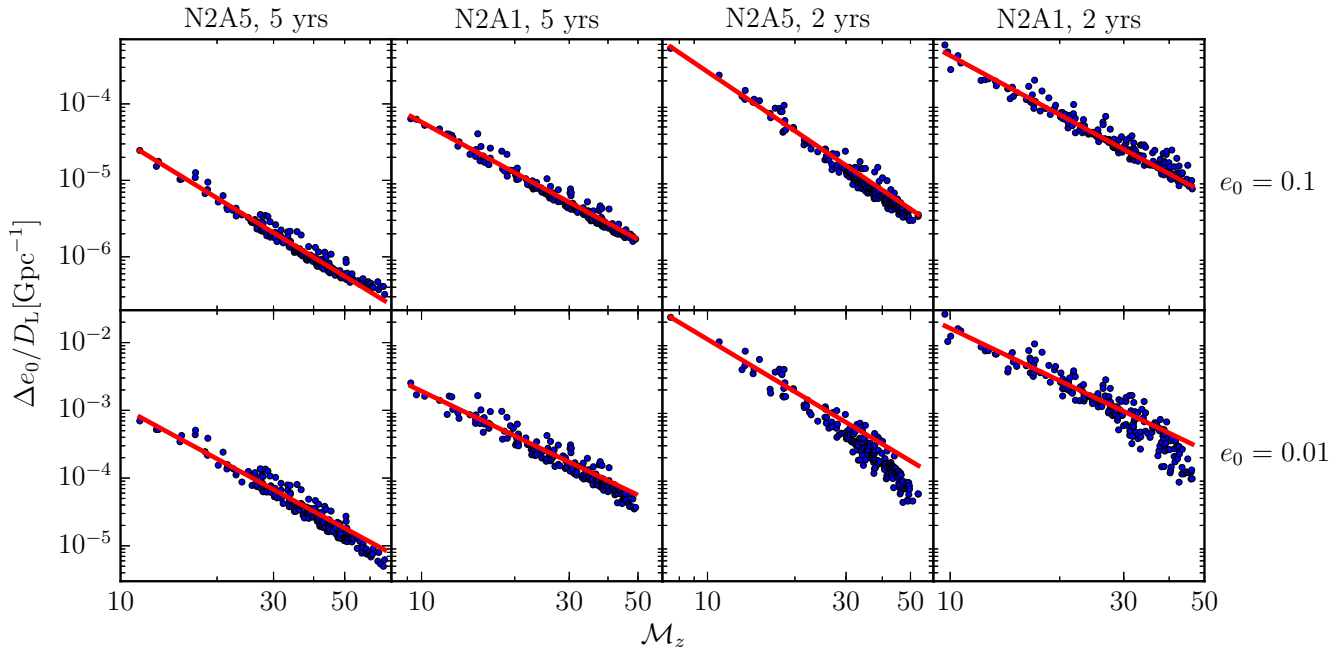


Figure 4. Scalings of parameter estimation errors $\Delta e_0/D_L$ with \mathcal{M}_z for full eccentric systems. From top to bottom: $e_0 = 0.1$, $e_0 = 0.01$, and from left to right: N2A5, 5 yrs; N2A5, 2 yrs; N2A1, 5 yrs; N2A1, 2 yrs. The blue circles represent every system in the catalog, and the thick red lines correspond to fits for the relation $\Delta e_0/D_L = A\mathcal{M}_z^{-\gamma_m}$.

chirp mass and e_0 increase. Since frequency sidebands break the correlation between parameters, parameter estimation errors decrease more rapidly with e_0 in the full eccentric case than in the restricted eccentric case. A best fit to our numerical results for Δe_0 yields the scaling relation of Eq. (5), which is compared against the data in Fig. 4. The accuracy of the scaling relation degrades for eLISA designs with shorter armlength and for shorter mission durations. The scattering of the data is also larger for small eccentricities, where correlations between e_0 and the other parameters are larger.

In Fig. 5 we compare the error on the merger time for full (left) and restricted (right) eccentric waveforms. This plot shows quite clearly that as we increase e_0 (bottom to top in each figure) the determination of t_c gets better in the full eccentric case, where the more complex waveform breaks the correlation between the parameters, but not in the restricted eccentric case. This general trend applies to all measurement errors, so in the following we focus on full eccentric waveforms.

In Fig. 6 we use full eccentric waveforms to compute parameter estimation errors on the chirp mass \mathcal{M} (top left), symmetric mass ratio η (top right), luminosity distance D_L (bottom left) and sky location $\Delta\Omega_S$ (bottom right) for full eccentric nonspinning binaries. The most notable feature of this plot is that the errors on the mass parameters decrease with e_0 , while the errors on source localization and distance are not sensibly affected by e_0 .

Looking at the sky location determination $\Delta\Omega_S$ in

Fig. 6, a careful reader will notice the seemingly counterintuitive result that binaries observed for 5 years will be located with worse precision than binaries observed for 2 years. This is simply a selection effect. Our catalogs were constructed by imposing an SNR threshold of $\rho > 8$, therefore catalogs corresponding to shorter observation times include systems with smaller luminosity distance and more optimal orientation. To show that selection effects are indeed responsible for this counterintuitive trend, in Fig. 7 we plot histograms of the angular resolution accuracy rescaled by the luminosity distance D_L . When normalized to D_L , the angular resolution distributions for the 5-year catalogs are indeed almost indistinguishable from those computed for the 2-year catalogs.

V. DISCUSSION

In this section we discuss how our parameter estimation calculations would change if we were to relax some of the approximations involved in our waveform models and parameter estimation techniques. In particular, we focus on the effect of high eccentricity, spins, confusion noise, and the Fisher matrix approximation.

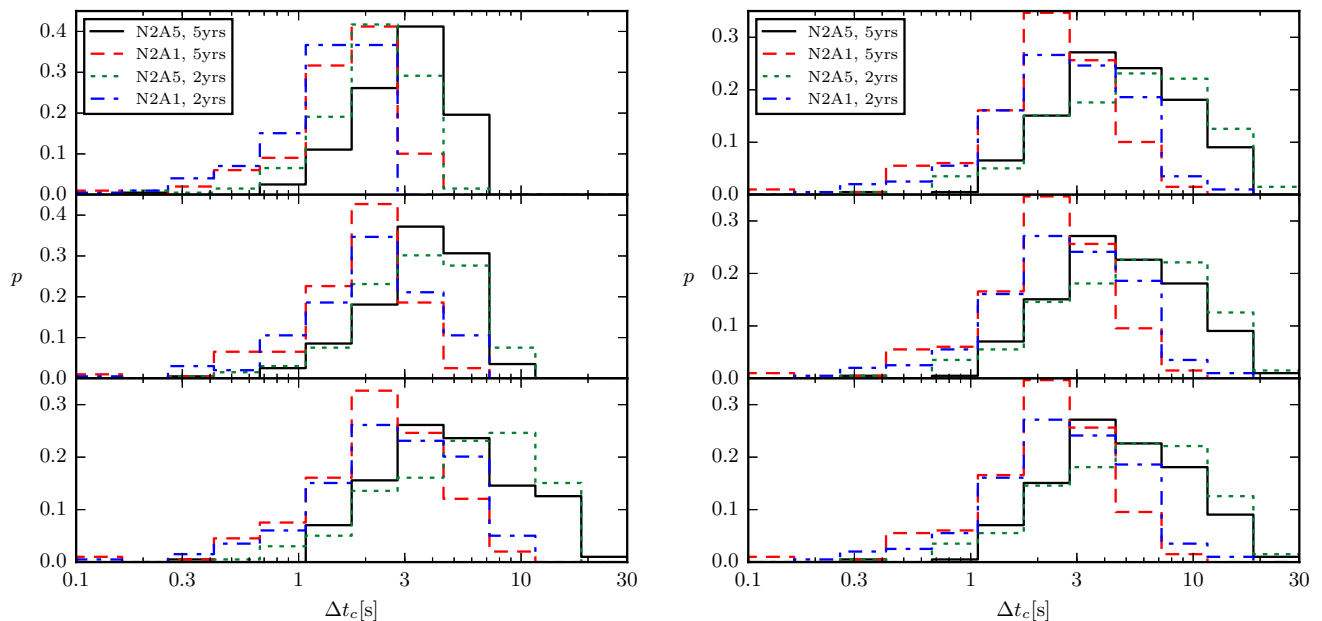


Figure 5. Parameter estimation errors on the time of coalescence Δt_c for full eccentric (left) and restricted eccentric (right) nonspinning binaries. On the top, systems with $e_0 = 0.1$, in the middle, systems with $e_0 = 0.01$, and at the bottom, systems with $e_0 = 0.001$. In solid black, N2A5 with $T_{\text{obs}} = 5$ yrs, in dashed red, N2A1 with $T_{\text{obs}} = 5$ yrs, in dotted green, N2A5 with $T_{\text{obs}} = 2$ yrs, in dash-dotted blue, N2A1 with $T_{\text{obs}} = 2$ yrs.

A. Highly eccentric binaries

One important limitation of our approach is the small- e_0 expansion adopted in our waveform models. All BH binaries we consider are evolving in frequency above $f = 0.01$ Hz, and our results are accurate at the level of $\mathcal{O}(e_0^2)$. Expected astrophysical eccentricities for field binaries and binaries in a dense stellar cluster are $e_0 \lesssim 0.1$. For these populations our phasing is accurate to within $\sim 1\%$, so we expect our parameter estimation results to be representative of the capabilities of eLISA when more accurate waveforms will be available. For binary populations models which predict large numbers of binaries with $0.1 \lesssim e_0 < 1$, however, our small-eccentricity approximation is not good enough. In principle one could keep terms up to $\mathcal{O}(e_0^6)$ using currently available waveforms, but even the detection of highly eccentric ($e_0 \sim 1$) binaries requires nonperturbative (in e_0) eccentric waveform. The development of accurate high-eccentricity waveforms is a very active research area and it is beyond the scope of this study [19–26].

B. Spinning binaries

In this paper we considered nonspinning BH binaries, but the introduction of spin parameters in the full eccentric waveforms should not degrade parameter estimation accuracy. For binaries with aligned spins, spin effects

enter the waveform at 1.5PN order, while eccentricity enters the waveform at Newtonian level and it is proportional to $f^{-19/18}$. This implies that spin effects are more important at higher frequencies and eccentricity dominates at lower frequencies, so that degeneracies between spin and eccentricity effects should be small. In fact we have computed errors on e_0 for nonspinning and aligned-spin binaries using the “restricted” eccentric waveforms of Section III A, and confirmed that relative variations in the errors are below 60% (in the worst cases) for all eLISA configurations considered in this study.

C. Confusion noise

If many binaries emit in a given observational frequency band, their signal will constitute a source of confusion noise that can limit detectability and parameter estimation accuracy. A simple estimate of this confusion noise is given in Appendix A, and it allows us to conclude that our signals are unlikely to be contaminated by confusion noise. To verify this statement we can compare the typical starting frequency of a BH binary for a given eLISA observation time with the “confusion noise frequency” below which more than two GW signals exist simultaneously in a single frequency bin. The former is 2.1×10^{-2} Hz (1.5×10^{-2} Hz) for 2-year (5-year) eLISA observations, respectively. Using Eq. (A5), the confusion noise frequency can be estimated to be 1.1×10^{-2} Hz

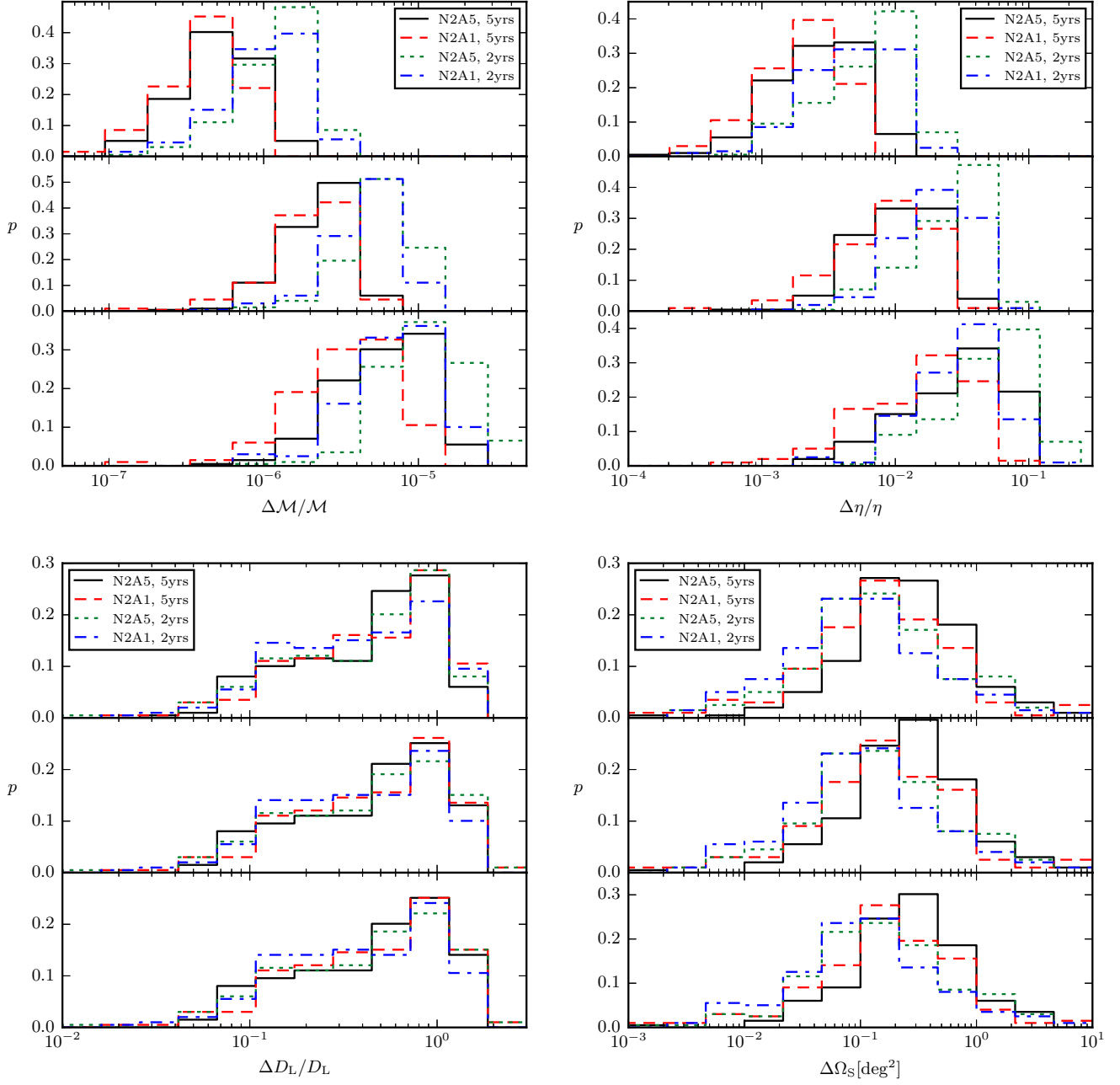


Figure 6. Parameter estimation errors on the chirp mass \mathcal{M} (top left), symmetric mass ratio (top right), luminosity distance D_L (bottom left) and sky location $\Delta\Omega_S$ (bottom right) for full eccentric nonspinning binaries. On the top, systems with $e_0 = 0.1$, in the middle, systems with $e_0 = 0.01$, and at the bottom, systems with $e_0 = 0.001$. In solid black, N2A5 with $T_{\text{obs}} = 5$ yrs, in dashed red, N2A1 with $T_{\text{obs}} = 5$ yrs, in dotted green, N2A5 with $T_{\text{obs}} = 2$ yrs, in dash-dotted blue, N2A1 with $T_{\text{obs}} = 2$ yrs.

(8.4×10^{-3} Hz) for a typical BH binary merger rate of $30 \text{ Gpc}^{-3} \text{ yr}^{-1}$ and 2-year (5-year) eLISA observations, respectively. Therefore, in general, the signal should be relatively easy to resolve and disentangle in the frequency region of interest for multiband binaries. In principle extreme mass ratio inspirals may overlap in frequency with some multiband binaries, but their waveform is expected

to be quite different (because of high eccentricity and spin precession). Note, moreover, that we do not expect significant contributions to confusion noise from other galactic sources (such as WD-WD binaries) at the frequencies of interest.

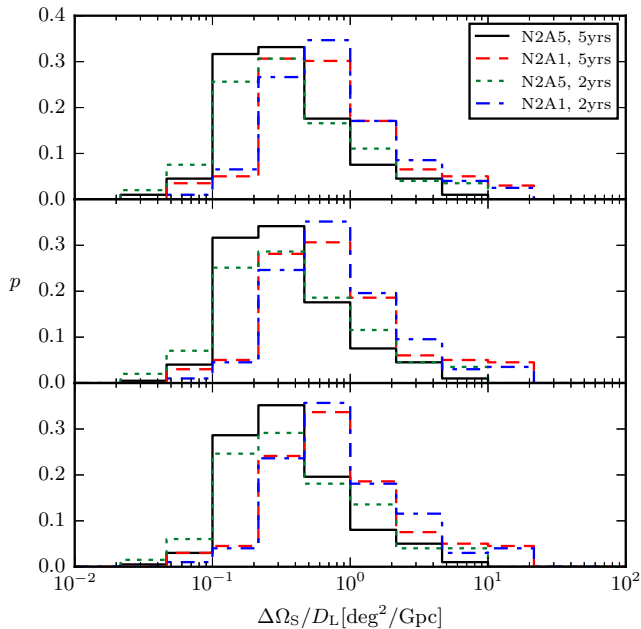


Figure 7. Distribution of $\Delta\Omega_S/D_L$ illustrating selection effects.

D. Fisher matrix analysis

The Fisher matrix approximation is well known to break down for low-SNR systems (see e.g. [91]). A comparison of Fisher-matrix results with Markov-Chain Monte Carlo results can be found in [92]. Their study focuses on Advanced LIGO, but their typical SNRs ($\sim 10 - 20$) are similar to those of interest in our work. Ref. [92] shows that there Fisher-matrix parameter estimation results have large scatter, but median values are relatively robust. In this sense, our Fisher analysis should be relatively reliable for Monte-Carlo studies of source populations.

In the LISA context, parameter estimation studies beyond the Fisher matrix approximation were implemented in some studies of WD binaries and EMRIs, most notably in the Mock LISA Data Challenges [93, 94]. Some results of those studies concern low SNR sources that remain in band for a long time, and they support the validity of our analysis. The data challenge is to dig out the signal from the data by matching a sufficient number of cycles, but once a signal is detected, the precision to which the parameters are estimated is comparable to Fisher matrix estimates. This has been demonstrated both for galactic WDs (similar to BH binary signals that hardly evolve in frequency during the eLISA observation, i.e. those at frequencies $f < 10^{-2}$ Hz) and for EMRIs (similar to massive BH signals chirping and “crossing over” to the Advanced LIGO band at $f > 10^{-2}$ Hz). In both cases, once the signal is above the detection threshold (usually assumed to be SNR= 7 for WD binaries and SNR= 15 – 20 for

EMRIs), parameters are estimated with very high precision and usually also with good accuracy. In a few cases, EMRI parameters are not accurately recovered because of failures in identifying the global maximum in the likelihood function, but this is an issue related to the search algorithms: the likelihood function exploration fails to correctly identify the sources. This issue is unlikely to be as relevant here, since BH binary eccentricities are usually small, implying a smoother behavior of the likelihood function (prominent secondary maxima associated to strong higher harmonics of the signal should be absent). In any case, both WD binary and EMRI parameters have been recovered with high accuracy and precision in the aforementioned numerical experiments, and the errors are not too far from Fisher Matrix estimates (usually within a factor of five in the worst cases).

VI. CONCLUSIONS

Binaries formed via dynamical interactions in dense star clusters are expected to be at least mildly eccentric ($e_0 \sim 10^{-3} - 10^{-1}$) at the frequencies $f_0 = 10^{-2}$ Hz where eLISA is most sensitive [74]. On the contrary, binaries formed in the field are expected to have negligible eccentricities ($e_0 \sim 10^{-6} - 10^{-4}$) in the eLISA band [58]. In this paper we carried out Monte Carlo simulations over a catalog of BH binaries that merge in the Advanced LIGO band to assess eLISA’s potential to measure eccentricity, and therefore differentiate between competing BH formation scenarios. We showed that eLISA should always be able to detect a nonzero e_0 whenever $e_0 \gtrsim 10^{-2}$. If $e_0 \sim 10^{-3}$, eLISA will detect nonzero eccentricity for a fraction $\sim 90\%$ ($\sim 25\%$) of binaries when the observation time is $T_{\text{obs}} = 5$ (2) years, respectively. Therefore eLISA observations of BH binaries have the potential to distinguish between field and cluster formation scenarios.

In the future we plan to refine this analysis using better waveform models and more realistic astrophysical assumptions. It is particularly interesting to consider binaries inspiralling at lower frequencies: these binaries will not necessarily “cross over” to the band accessible by Earth-based detectors, but they may have higher eccentricity, e.g. because of the Kozai mechanism [78–82]. These highly eccentric systems present a harder challenge in terms of data analysis, and they motivate further efforts to develop accurate waveform models and reliable parameter estimation schemes.

Appendix A: Confusion noise

At low frequencies the frequency evolution of a binary is slower, and the number of sources in a given frequency bin is larger. If there are more than two signals simultaneously in a single bin, these signals are indistinguishable and can produce confusion noise. In this Appendix we

estimate this effect, and we show that confusion noise is unlikely to affect our conclusions.

The number of inspiral GW signals $\Delta N(f)$ in a bin of frequency resolution $\Delta f = 1/T_{\text{obs}}$ is given by

$$\Delta N(f) = \frac{dN}{dt} \left(\frac{df}{dt} \right)^{-1} \Delta f. \quad (\text{A1})$$

Here dN/dt is the merger rate per unit time, which can be obtained by integrating over redshift:

$$\frac{dN}{dt} = \int dz \frac{d^2 N}{dz dt} = \int \frac{4\pi\chi^2(z)}{(1+z)H(z)} \dot{n}(z) dz, \quad (\text{A2})$$

where $\chi(z)$ is the comoving distance to redshift z , and $\dot{n}(z)$ is the merger rate per unit comoving volume and unit proper time at redshift z . For a constant merger rate $\dot{n}(z) = \dot{n}_0$, Eq. (A2) reduces to

$$\frac{dN}{dt} = \dot{n}_0 V, \quad V \equiv \int \frac{4\pi\chi^2(z)}{(1+z)H(z)} dz.$$

Substituting the frequency derivative at Newtonian order [95]

$$\frac{df}{dt} = \frac{96}{5} \pi^{8/3} \mathcal{M}_z^{5/3} f^{11/3}$$

into Eq. (A1), we have

$$\Delta N(f) = \frac{5}{96} \pi^{-8/3} \dot{n}_0 V \mathcal{M}_z^{-5/3} f^{-11/3} T_{\text{obs}}^{-1}.$$

For a power-law mass distribution of the form

$$p(\mathcal{M}) = \frac{\mathcal{M}^{-\alpha}}{\int_{\mathcal{M}_{\text{min}}}^{\mathcal{M}_{\text{max}}} (\mathcal{M}')^{-\alpha} d\mathcal{M}'}$$

the number of inspiral GW signals $\Delta N(f)$ should be replaced with the averaged value

$$\langle \Delta N(f) \rangle = \frac{5}{96} \pi^{-8/3} \dot{n}_0 V \langle \mathcal{M}_z^{-5/3} \rangle f^{-11/3} T_{\text{obs}}^{-1}, \quad (\text{A3})$$

where

$$\begin{aligned} \langle \mathcal{M}_z^{-5/3} \rangle &= \langle (1+z)^{-5/3} \mathcal{M}^{-5/3} \rangle \\ &= \langle (1+z)^{-5/3} \rangle \int d\mathcal{M} \mathcal{M}^{-5/3} p(\mathcal{M}) \\ &= \frac{3(\alpha-1)}{3\alpha+2} \langle (1+z)^{-5/3} \rangle \frac{\mathcal{M}_{\text{max}}^{-\alpha-2/3} - \mathcal{M}_{\text{min}}^{-\alpha-2/3}}{\mathcal{M}_{\text{max}}^{1-\alpha} - \mathcal{M}_{\text{min}}^{1-\alpha}} \end{aligned}$$

and (assuming that $\alpha \neq 1$)

$$\begin{aligned} \langle (1+z)^{-5/3} \rangle &= \int_0^\infty dz \frac{dV/dz}{V} (1+z)^{-5/3} \\ &= \frac{1}{V} \int_0^\infty dz \frac{4\pi\chi^2(z)}{(1+z)^{8/3} H(z)}. \end{aligned}$$

For a log-flat mass distribution ($\alpha = 1$) we would get instead

$$\langle \mathcal{M}_z^{-5/3} \rangle_{\alpha=1} = \frac{3}{5} \langle (1+z)^{-5/3} \rangle \frac{\mathcal{M}_{\text{min}}^{-5/3} - \mathcal{M}_{\text{max}}^{-5/3}}{\ln[\mathcal{M}_{\text{max}}/\mathcal{M}_{\text{min}}]}.$$

Setting $\langle \Delta N(f_{\text{conf}}) \rangle = 1$ in Eq. (A3), we obtain the critical frequency below which more than two signals are in the same frequency bin:

$$f_{\text{conf}} = \left(\frac{5 \dot{n}_0 V}{96 T_{\text{obs}}} \right)^{3/11} \pi^{-8/11} \langle \mathcal{M}_z^{-5/3} \rangle^{3/11}. \quad (\text{A4})$$

This is the main result of this appendix. For a Λ CDM cosmology with $\Omega_m = 0.3$, $\Omega_\Lambda = 1 - \Omega_m$, and $H_0 = 72 \text{ km s}^{-1} \text{ Mpc}^{-1}$ [86] and for the astrophysical population considered in this paper, the averaged quantities are $\langle (1+z)^{-5/3} \rangle \approx 0.121$ and $\langle \mathcal{M}_z^{-5/3} \rangle_{\alpha=1}^{-3/5} \approx 35 M_\odot$ (where for simplicity we set $\eta = 1/4$). Then the confusion noise frequency is

$$\begin{aligned} f_{\text{conf}} &\approx 8.4 \times 10^{-3} \left(\frac{5 \text{ yr}}{T_{\text{obs}}} \right)^{3/11} \left(\frac{\dot{n}_0}{30 \text{ Gpc}^{-3} \text{ yr}^{-1}} \right)^{3/11} \\ &\times \left(\frac{35 M_\odot}{\langle \mathcal{M}_z^{-5/3} \rangle^{-3/5}} \right)^{5/11} \text{ Hz}. \quad (\text{A5}) \end{aligned}$$

It is useful to estimate the confusion noise power spectrum: even if there is confusion noise in a given frequency band, its effects can be ignored as long as the confusion noise amplitude is much smaller than the detector strain sensitivity. The energy density of GWs per logarithmic frequency bin normalized by the critical energy density of the Universe at the present time can be written as [96]

$$\Omega_{\text{gw}}(f) = \frac{8\pi^{5/3}}{9H_0^2} \mathcal{M}^{5/3} f^{2/3} \int_0^\infty \frac{\dot{n}(z)}{(1+z)^{4/3} H(z)} dz.$$

Using the relation between Ω_{gw} and the power spectral density [97]

$$\Omega_{\text{gw}}(f) = \frac{4\pi^2 f^3}{3H_0^2} S_h(f),$$

we get the confusion noise power spectral density

$$S_h^{\text{conf}}(f) = \frac{2}{3\pi^{1/3}} \mathcal{M}^{5/3} f^{-7/3} \int_0^\infty \frac{\dot{n}(z)}{(1+z)^{4/3} H(z)} dz.$$

For a power-law mass distribution, \mathcal{M} should be replaced with the averaged value

$$\begin{aligned} \langle \mathcal{M}^{5/3} \rangle &= \int d\mathcal{M} \mathcal{M}^{5/3} p(\mathcal{M}) \\ &= \frac{3(1-\alpha)}{8-3\alpha} \frac{\mathcal{M}_{\text{max}}^{8/3-\alpha} - \mathcal{M}_{\text{min}}^{8/3-\alpha}}{\mathcal{M}_{\text{max}}^{1-\alpha} - \mathcal{M}_{\text{min}}^{1-\alpha}}, \end{aligned}$$

where we assumed $\alpha \neq 1$. Using a log-flat mass distribution ($\alpha = 1$) yields instead

$$\langle \mathcal{M}^{5/3} \rangle_{\alpha=1} = \frac{3}{5} \frac{\mathcal{M}_{\text{max}}^{5/3} - \mathcal{M}_{\text{min}}^{5/3}}{\ln[\mathcal{M}_{\text{max}}/\mathcal{M}_{\text{min}}]}.$$

For the astrophysical populations we consider, the averaged quantities are $\langle \mathcal{M}^{5/3} \rangle_{\alpha=1}^{3/5} \approx 19 M_{\odot}$ and $\langle \mathcal{M}^{5/3} \rangle_{\alpha=2.35}^{3/5} \approx 11 M_{\odot}$ (once again, for simplicity, we set $\eta = 1/4$). Assuming a constant merger rate $\dot{n}(z) = \dot{n}_0$, the confusion noise power spectrum is

$$S_h^{\text{conf}}(f) = 1.2 \times 10^{-42} \left(\frac{10^{-2} \text{ Hz}}{f} \right)^{7/3} \left(\frac{\dot{n}_0}{30 \text{ Gpc}^{-3} \text{ yr}^{-1}} \right) \times \left(\frac{\langle \mathcal{M}^{5/3} \rangle^{3/5}}{19 M_{\odot}} \right) \text{ Hz}^{-1}, \quad (\text{A6})$$

or

$$\Omega_{\text{gw}}(f) = 2.8 \times 10^{-12} \left(\frac{f}{10^{-2} \text{ Hz}} \right)^{2/3} \left(\frac{\dot{n}_0}{30 \text{ Gpc}^{-3} \text{ yr}^{-1}} \right) \times \left(\frac{\langle \mathcal{M}^{5/3} \rangle^{3/5}}{19 M_{\odot}} \right). \quad (\text{A7})$$

Using the typical parameters considered in this paper, we conclude that the confusion noise is smaller than the eLISA noise power spectral density at frequencies above 10^{-2} Hz. At frequencies lower than 10^{-2} Hz some contamination from confusion noise is possible, depending on eLISA design choices.

ACKNOWLEDGMENTS

E.B., A.K. and A.N. are supported by NSF CAREER Grant No. PHY-1055103 and by NSF Grant No. PHY-1607130. E.B. and A.K. are supported by FCT contract IF/00797/2014/CP1214/CT0012 under the IF2014 Programme. A.S. is supported by a University Research Fellowship of the Royal Society. This work was supported by the H2020-MSCA-RISE-2015 Grant No. StronGrHEP-690904.

-
- [1] B. P. Abbott *et al.* (Virgo, LIGO Scientific), Phys. Rev. Lett. **116**, 061102 (2016), arXiv:1602.03837 [gr-qc].
- [2] B. P. Abbott *et al.* (Virgo, LIGO Scientific), (2016), arXiv:1602.03840 [gr-qc].
- [3] B. P. Abbott *et al.* (Virgo, LIGO Scientific), (2016), arXiv:1602.03842 [astro-ph.HE].
- [4] B. P. Abbott *et al.* (Virgo, LIGO Scientific), Astrophys. J. **818**, L22 (2016), arXiv:1602.03846 [astro-ph.HE].
- [5] K. A. Postnov and L. R. Yungelson, Living Rev. Rel. **17**, 3 (2014), arXiv:1403.4754 [astro-ph.HE].
- [6] M. J. Benacquista and J. M. B. Downing, Living Rev. Rel. **16**, 4 (2013), arXiv:1110.4423 [astro-ph.SR].
- [7] A. Sesana, Phys. Rev. Lett. **116**, 231102 (2016), arXiv:1602.06951 [gr-qc].
- [8] P. Amaro-Seoane *et al.*, GW Notes **6**, 4 (2013), arXiv:1201.3621 [astro-ph.CO].
- [9] B. P. Abbott *et al.* (Virgo, LIGO Scientific), (2016), arXiv:1602.03841 [gr-qc].
- [10] N. Yunes, K. Yagi, and F. Pretorius, (2016), arXiv:1603.08955 [gr-qc].
- [11] E. Barausse, N. Yunes, and K. Chamberlain, (2016), arXiv:1603.04075 [gr-qc].
- [12] D. Gerosa, M. Kesden, E. Berti, R. O’Shaughnessy, and U. Sperhake, Phys. Rev. **D87**, 104028 (2013), arXiv:1302.4442 [gr-qc].
- [13] P. Amaro-Seoane, M. C. Miller, and M. Freitag, Astrophys. J. **692**, L50 (2009), arXiv:0901.0604 [astro-ph.SR].
- [14] P. Amaro-Seoane, C. Eichhorn, E. Porter, and R. Spurzem, Mon. Not. Roy. Astron. Soc. **401**, 2268 (2010), arXiv:0908.0755 [astro-ph.GA].
- [15] P. Amaro-Seoane and L. Santamaria, Astrophys. J. **722**, 1197 (2010), arXiv:0910.0254 [astro-ph.CO].
- [16] N. Seto, (2016), 10.1093/mnras/171/3/060, arXiv:1602.04715 [astro-ph.HE].
- [17] N. Yunes, K. G. Arun, E. Berti, and C. M. Will, Phys. Rev. **D80**, 084001 (2009), [Erratum: Phys. Rev. **D89**, no.10, 109901 (2014)], arXiv:0906.0313 [gr-qc].
- [18] S. Tanay, M. Haney, and A. Gopakumar, Phys. Rev. **D93**, 064031 (2016), arXiv:1602.03081 [gr-qc].
- [19] K. Martel and E. Poisson, Phys. Rev. **D60**, 124008 (1999), arXiv:gr-qc/9907006 [gr-qc].
- [20] B. Mikoczi, B. Kocsis, P. Forgacs, and M. Vasuth, Phys. Rev. **D86**, 104027 (2012), arXiv:1206.5786 [gr-qc].
- [21] E. Huerta, P. Kumar, S. T. McWilliams, R. O’Shaughnessy, and N. Yunes, Phys. Rev. **D90**, 084016 (2014), arXiv:1408.3406 [gr-qc].
- [22] B. Sun, Z. Cao, Y. Wang, and H.-C. Yeh, Phys. Rev. **D92**, 044034 (2015).
- [23] E. Forseth, C. R. Evans, and S. Hopper, Phys. Rev. **D93**, 064058 (2016), arXiv:1512.03051 [gr-qc].
- [24] S. Hopper, C. Kavanagh, and A. C. Ottewill, Phys. Rev. **D93**, 044010 (2016), arXiv:1512.01556 [gr-qc].
- [25] B. Moore, M. Favata, K. G. Arun, and C. K. Mishra, (2016), arXiv:1605.00304 [gr-qc].
- [26] N. Loutrel and N. Yunes, (2016), arXiv:1607.05409 [gr-qc].
- [27] J. Abadie *et al.* (VIRGO, LIGO Scientific), Class. Quant. Grav. **27**, 173001 (2010), arXiv:1003.2480 [astro-ph.HE].
- [28] S. Stevenson, F. Ohme, and S. Fairhurst, Astrophys. J. **810**, 58 (2015), arXiv:1504.07802 [astro-ph.HE].
- [29] A. Tutukov and L. Yungelson, Nauchnye Informatsii **27**, 70 (1973).
- [30] A. V. Tutukov and L. R. Yungelson, Mon. Not. Roy. Astron. Soc. **260**, 675 (1993).
- [31] V. M. Lipunov, K. A. Postnov, and M. E. Prokhorov, Mon. Not. Roy. Astron. Soc. **288**, 245 (1997), arXiv:astro-ph/9702060 [astro-ph].
- [32] H. A. Bethe and G. E. Brown, Astrophys. J. **506**, 780 (1998), arXiv:astro-ph/9802084 [astro-ph].
- [33] L. P. Grishchuk, V. M. Lipunov, K. A. Postnov, M. E. Prokhorov, and B. S. Sathyaprakash, Phys. Usp. **44**, 1 (2001), [Usp. Fiz. Nauk171,3(2001)], arXiv:astro-ph/0008481 [astro-ph].
- [34] G. Nelemans, L. R. Yungelson, and S. F. Portegies Zwart, Astron. Astrophys. **375**, 890 (2001), arXiv:astro-ph/0105221 [astro-ph].
- [35] K. Belczynski, V. Kalogera, and T. Bulik, Astrophys. J. **572**, 407 (2001), arXiv:astro-ph/0111452 [astro-ph].

- [36] R. Voss and T. M. Tauris, *Mon. Not. Roy. Astron. Soc.* **342**, 1169 (2003), arXiv:astro-ph/0303227 [astro-ph].
- [37] E. De Donder and D. Vanbeveren, *New Astron. Rev.* **48**, 861 (2004), arXiv:astro-ph/0410024 [astro-ph].
- [38] K. Belczynski, V. Kalogera, F. A. Rasio, R. E. Taam, A. Zezas, T. Bulik, T. J. Maccarone, and N. Ivanova, *Astrophys. J. Suppl.* **174**, 223 (2008), arXiv:astro-ph/0511811 [astro-ph].
- [39] R. W. O’Shaughnessy, C. Kim, V. Kalogera, and K. Belczynski, *Astrophys. J.* **672**, 479 (2008), arXiv:astro-ph/0610076 [astro-ph].
- [40] V. Kalogera, K. Belczynski, C. Kim, R. W. O’Shaughnessy, and B. Willems, *Phys. Rept.* **442**, 75 (2007), arXiv:astro-ph/0612144 [astro-ph].
- [41] N. Mennekens and D. Vanbeveren, *Astron. Astrophys.* **564**, A134 (2014), arXiv:1307.0959 [astro-ph.SR].
- [42] K. Belczynski, M. Dominik, T. Bulik, R. O’Shaughnessy, C. L. Fryer, and D. E. Holz, *Astrophys. J.* **715**, L138 (2010), arXiv:1004.0386 [astro-ph.HE].
- [43] M. Dominik, K. Belczynski, C. Fryer, D. Holz, E. Berti, T. Bulik, I. Mandel, and R. O’Shaughnessy, *Astrophys. J.* **759**, 52 (2012), arXiv:1202.4901 [astro-ph.HE].
- [44] M. Dominik, K. Belczynski, C. Fryer, D. E. Holz, E. Berti, T. Bulik, I. Mandel, and R. O’Shaughnessy, *Astrophys. J.* **779**, 72 (2013), arXiv:1308.1546 [astro-ph.HE].
- [45] K. Belczynski, A. Buonanno, M. Cantiello, C. L. Fryer, D. E. Holz, I. Mandel, M. C. Miller, and M. Walczak, *Astrophys. J.* **789**, 120 (2014), arXiv:1403.0677 [astro-ph.HE].
- [46] M. Dominik, E. Berti, R. O’Shaughnessy, I. Mandel, K. Belczynski, C. Fryer, D. Holz, T. Bulik, and F. Panarale, *Astrophys. J.* **806**, 263 (2015), arXiv:1405.7016 [astro-ph.HE].
- [47] K. Belczynski, S. Repetto, D. E. Holz, R. O’Shaughnessy, T. Bulik, E. Berti, C. Fryer, and M. Dominik, *Astrophys. J.* **819**, 108 (2016), arXiv:1510.04615 [astro-ph.HE].
- [48] K. Belczynski, D. E. Holz, T. Bulik, and R. O’Shaughnessy, (2016), arXiv:1602.04531 [astro-ph.HE].
- [49] M. Spera, M. Mapelli, and A. Bressan, *Mon. Not. Roy. Astron. Soc.* **451**, 4086 (2015), arXiv:1505.05201 [astro-ph.SR].
- [50] J. J. Eldridge and E. R. Stanway, (2016), arXiv:1602.03790 [astro-ph.HE].
- [51] I. Mandel and S. E. de Mink, (2015), 10.1093/mnras/stw379, arXiv:1601.00007 [astro-ph.HE].
- [52] S. E. de Mink and I. Mandel, (2016), arXiv:1603.02291 [astro-ph.HE].
- [53] P. Marchant, N. Langer, P. Podsiadlowski, T. Tauris, and T. Moriya, *Astron. Astrophys.* **588**, A50 (2016), arXiv:1601.03718 [astro-ph.SR].
- [54] T. Kinugawa, K. Inayoshi, K. Hotokezaka, D. Nakauchi, and T. Nakamura, *Mon. Not. Roy. Astron. Soc.* **442**, 2963 (2014), arXiv:1402.6672 [astro-ph.HE].
- [55] T. Kinugawa, A. Miyamoto, N. Kanda, and T. Nakamura, *Mon. Not. Roy. Astron. Soc.* **456**, 1093 (2016), arXiv:1505.06962 [astro-ph.SR].
- [56] K. Inayoshi, K. Kashiyama, E. Visbal, and Z. Haiman, (2016), arXiv:1603.06921 [astro-ph.GA].
- [57] T. Hartwig, M. Volonteri, V. Bromm, R. S. Klessen, E. Barausse, M. Magg, and A. Stacy, (2016), arXiv:1603.05655 [astro-ph.GA].
- [58] I. Kowalska, T. Bulik, K. Belczynski, M. Dominik, and D. Gondek-Rosinska, *Astron. Astrophys.* **527**, A70 (2011), arXiv:1010.0511 [astro-ph.CO].
- [59] S. F. Kulkarni, S. McMillan, and P. Hut, *Nature* **364**, 421 (1993).
- [60] S. Sigurdsson and L. Hernquist, *Nature* **364**, 423 (1993).
- [61] S. F. Portegies Zwart and S. McMillan, *Astrophys. J.* **528**, L17 (2000), arXiv:astro-ph/9910061 [astro-ph].
- [62] M. A. Gurkan, J. M. Fregeau, and F. A. Rasio, *Astrophys. J.* **640**, L39 (2006), arXiv:astro-ph/0512642 [astro-ph].
- [63] K. Gültekin, M. C. Miller, and D. P. Hamilton, *Astrophys. J.* **640**, 156 (2006), astro-ph/0509885.
- [64] J. M. Fregeau, S. L. Larson, M. C. Miller, R. W. O’Shaughnessy, and F. A. Rasio, *Astrophys. J.* **646**, L135 (2006), arXiv:astro-ph/0605732 [astro-ph].
- [65] M. C. Miller and V. M. Lauburg, *Astrophys. J.* **692**, 917 (2009), arXiv:0804.2783 [astro-ph].
- [66] R. M. O’Leary, B. Kocsis, and A. Loeb, *Mon. Not. Roy. Astron. Soc.* **395**, 2127 (2009), arXiv:0807.2638 [astro-ph].
- [67] K. Moody and S. Sigurdsson, *Astrophys. J.* **690**, 1370 (2009), arXiv:0809.1617 [astro-ph].
- [68] J. M. B. Downing, M. J. Benacquista, M. Giersz, and R. Spurzem, *Mon. Not. Roy. Astron. Soc.* **407**, 1946 (2010), arXiv:0910.0546 [astro-ph.SR].
- [69] J. M. B. Downing, M. J. Benacquista, M. Giersz, and R. Spurzem, *Mon. Not. Roy. Astron. Soc.* **416**, 133 (2011), arXiv:1008.5060.
- [70] M. Morscher, S. Umbreit, W. M. Farr, and F. A. Rasio, *Astrophys. J.* **763**, L15 (2013), arXiv:1211.3372 [astro-ph.GA].
- [71] S. Goswami, P. Kiel, and F. A. Rasio, *Astrophys. J.* **781**, 81 (2014), arXiv:1309.3703 [astro-ph.GA].
- [72] B. M. Ziosi, M. Mapelli, M. Branchesi, and G. Tormen, *Mon. Not. Roy. Astron. Soc.* **441**, 3703 (2014), arXiv:1404.7147 [astro-ph.GA].
- [73] C. L. Rodriguez, M. Morscher, B. Pattabiraman, S. Chatterjee, C.-J. Haster, and F. A. Rasio, *Phys. Rev. Lett.* **115**, 051101 (2015), [Erratum: *Phys. Rev. Lett.* **116**, no.2, 029901 (2016)], arXiv:1505.00792 [astro-ph.HE].
- [74] C. L. Rodriguez, S. Chatterjee, and F. A. Rasio, *Phys. Rev.* **D93**, 084029 (2016), arXiv:1602.02444 [astro-ph.HE].
- [75] R. M. O’Leary, Y. Meiron, and B. Kocsis, (2016), arXiv:1602.02809 [astro-ph.HE].
- [76] I. Bartos, B. Kocsis, Z. Haiman, and S. Márka, (2016), arXiv:1602.03831 [astro-ph.HE].
- [77] S. Chatterjee, C. L. Rodriguez, and F. A. Rasio, (2016), arXiv:1603.00884 [astro-ph.GA].
- [78] L. Wen, *Astrophys. J.* **598**, 419 (2003), arXiv:astro-ph/0211492 [astro-ph].
- [79] F. Antonini and H. B. Perets, *Astrophys. J.* **757**, 27 (2012), arXiv:1203.2938 [astro-ph.GA].
- [80] J. H. VanLandingham, M. C. Miller, D. P. Hamilton, and D. C. Richardson, (2016), arXiv:1604.04948 [astro-ph.HE].
- [81] F. Antonini, S. Chatterjee, C. L. Rodriguez, M. Morscher, B. Pattabiraman, V. Kalogera, and F. A. Rasio, *Astrophys. J.* **816**, 65 (2016), arXiv:1509.05080 [astro-ph.GA].
- [82] J. Samsing, M. MacLeod, and E. Ramirez-Ruiz, *Astrophys. J.* **784**, 71 (2014), arXiv:1308.2964 [astro-ph.HE].
- [83] P. C. Peters and J. Mathews, *Phys. Rev.* **131**, 435 (1963).

- [84] M. Enoki and M. Nagashima, *Prog. Theor. Phys.* **117**, 241 (2007), arXiv:astro-ph/0609377 [astro-ph].
- [85] A. Klein *et al.*, *Phys. Rev.* **D93**, 024003 (2016), arXiv:1511.05581 [gr-qc].
- [86] G. Hinshaw, D. Larson, E. Komatsu, D. N. Spergel, C. L. Bennett, J. Dunkley, M. R.olta, M. Halpern, R. S. Hill, N. Odegard, L. Page, K. M. Smith, J. L. Weiland, B. Gold, N. Jarosik, A. Kogut, M. Limon, S. S. Meyer, G. S. Tucker, E. Wollack, and E. L. Wright, *Astrophysical Journal Supplement Series* **208**, 19 (2013), arXiv:1212.5226.
- [87] A. Krolak, K. D. Kokkotas, and G. Schaefer, *Phys. Rev.* **D52**, 2089 (1995), arXiv:gr-qc/9503013 [gr-qc].
- [88] E. Berti, A. Buonanno, and C. M. Will, *Phys. Rev.* **D71**, 084025 (2005), arXiv:gr-qc/0411129 [gr-qc].
- [89] C. Cutler, *Phys. Rev.* **D57**, 7089 (1998), arXiv:gr-qc/9703068 [gr-qc].
- [90] S. A. Hughes, *Mon. Not. Roy. Astron. Soc.* **331**, 805 (2002), arXiv:astro-ph/0108483 [astro-ph].
- [91] M. Vallisneri, *Phys. Rev.* **D77**, 042001 (2008), arXiv:gr-qc/0703086 [GR-QC].
- [92] C. L. Rodriguez, B. Farr, W. M. Farr, and I. Mandel, *Phys. Rev.* **D88**, 084013 (2013), arXiv:1308.1397 [astro-ph.IM].
- [93] S. Babak *et al.* (Mock LISA Data Challenge Task Force), *Gravitational waves. Proceedings, 8th Edoardo Amaldi Conference, Amaldi 8, New York, USA, June 22-26, 2009*, *Class. Quant. Grav.* **27**, 084009 (2010), arXiv:0912.0548 [gr-qc].
- [94] A. Blaut, S. Babak, and A. Krolak, *Phys. Rev.* **D81**, 063008 (2010), arXiv:0911.3020 [gr-qc].
- [95] C. Cutler and E. E. Flanagan, *Phys. Rev.* **D49**, 2658 (1994), arXiv:gr-qc/9402014 [gr-qc].
- [96] E. S. Phinney, (2001), arXiv:astro-ph/0108028 [astro-ph].
- [97] M. Maggiore, *Phys. Rept.* **331**, 283 (2000), arXiv:gr-qc/9909001 [gr-qc].